RSC Advances

RSC Advances

www.rsc.org/advances

ROYAL SOCIETY OF CHEMISTRY

www.rsc.org/advances

Journal Name

RSC Advances

Dynamic Article Links ▶

ARTICLE TYPE

Facile synthesis of flower-like CoMn₂O₄ microspheres for electrochemical supercapacitors

Long Ren[1], Jun Chen[1], Xiaoqing Wang[2], Mingjia Zhi[3], Junwei Wu[1]*, Xinhe Zhang[4]

Facile synthesis of porous and hollow spinel materials is highly desirable for their extensive applications in energy storage fields. In this work, uniform and decentralized flower-like CoMn₂O₄ microspheres were synthesized and characterized for supercapacitor electrodes in neutral aqueous electrolyte. In this contribution, uniform microspheres precursors were firstly fabricated by solvothermal method, following by a
10 low temperature calcination process for crystallization. A detailed study shows that the deionized (DI) water content plays an important role in the solvothermal process to optimize the morphology of microspheres. In 1 M Na₂SO₄, the spinel electrode material owns a working potential window as high as 1.1 V and a specific capacitance of 188 F g⁻¹. Besides, the electrode material exhibits excellent cycling stability by retaining 93% of their original capacitance after 1000 cycles. Therefore, the flower-like microspheres
15 of CoMn₂O₄ spinel is a promising candidate for supercapacitor applications.

Introduction

Supercapacitor, also called electrochemical capacitor, has attracted comprehensive research attentions in recent years for its predominant properties, which include environmental friendly,
20 excellent cycle stability, higher power density and stable performance in a wide temperature scope [1-3]. Supercapacitors are usually classified into two categories based the energy storage mechanisms: electrical double-layer capacitor (EDLC) and pseudocapacitor [4, 5]. EDLCs store energy through the accumul-
25 ating of electric charge at the interface between electrode and electrolyte [6-9]. Pseudocapacitor stores energy by fast redox charge transferring, which can provide higher capacitance than EDLCs [10, 11]. Transition metal oxides are considered as ideal pseudocapacitors electrode materials for their varieties of cation
30 charges, such as MnO_2 [12], Co_3O_4 [13], Fe_3O_4 [14], and so on.

Surface properties of electrode materials are important factors for the specific capacitance of supercapacitors [15]. Carbon material is one of the most researched materials leading to unique and ideal microstructure. Compared with carbon materials, the
35 tailoring of specific morphology is difficult for metal oxides. Nowadays, many binary transition-metal oxides with spinel structure, such as $CuCo_2O_4$ [16], $ZnCo_2O_4$ [17], $NiCo_2O_4$ [18], $ZnMn_2O_4$ [19] and $CoMn_2O_4$ [20], etc, have been investigated as electrodes materials for energy storing. Wu et al. synthesized
40 mesoporous $Ni_{0.3}Co_{2.7}O_4$ with a high specific capacitance of 960 F g⁻¹ and excellent cyclic stability [21]. Compared with sole cation metal oxide, the spinel materials, which can provide superior electrochemical performances by forming specific structure and charge transfer modes, are desirable in supercapacitors
45 applications. Among the spinels, Mn-Co oxide has been used promisingly as supercapacitor electrode due to the high capacitance and richer redox reactions over unitary Mn or Co

oxide. Xu et al. synthesized $CoMn_2O_4$ and $MnCo_2O_4$ nanowires by thermal decomposition of organometallic compounds, both of
50 them showed high specific capacitance in 2 M KOH electrolyte [22]. Zou et al. reported the urchin-like $MnCo_2O_4$ with hierarchical architectures showed a specific capacitance of 151.2 F g⁻¹ at 5 mV s⁻¹ in 1 M KOH solution [23]. By far, most of the related work was characterized in alkaline electrolyte. Comparatively, the
55 neutral electrolyte has the advantage of low cost, non-corrosive and allow applying diverse current collectors, which makes the assembling process much easier and cheaper and the supercapacitor more environmentally friendly [24]. Additionally, neutral electrolytes are benefit for stable electrochemical process
60 with higher potential window [25] and better cycle performance can be achieved. For the spinel material $CoMn_2O_4$, despite the obviously redox nature of the energy storage mechanism, fast ion adsorption on electrode surface can be considered as another feasible energy storage mechanism.

65 In this work, novel flower-like $CoMn_2O_4$ microspheres were synthesized by solvothermal method as electrode materials for supercapacitor applications. We acquired the Co/Mn-EG (Ethylene glycol salt) precursors first [26], followed by a calcination process to complete the phase transformation of
70 $CoMn_2O_4$. A facile route was developed to optimize the microsphere morphology by adding a small amount of DI water, finally achieved the flower-like microspheres. In the following calcinations process, a comparatively low temperature of 300 ℃ is sufficient for the phase transformation with high performance.
75 The supercapacitor properties are evaluated by electrochemical methods in neutral electrolyte of 1 M Na₂SO₄.

Experimental

Synthesis of flower-like CoMn₂O₄ microspheres

Ethylene glycol (HOC$_2$H$_4$OH, GC 99%), Mn(CH$_3$COO)$_2$·4H$_2$O ，Co(CH$_3$COO)$_2$·4H$_2$O and polyethylene glycol (PEG) 1000 were supplied by Shanghai Aladdin Chemical Reagent Co. Ltd. All chemicals were used as received without further purification. Except ethylene glycol, all other chemicals were of analytical grade.

In a typical procedure, 0.248g Co(CH$_3$COO)$_2$·4H$_2$O (1 mmol), 0.49g Mn(CH$_3$COO)$_2$·4H$_2$O (2 mmol) and 1 g PEG 1000 were completely dissolved in 70 ml ethylene glycol (EG) under stirring in 50 ^{o}C water bath, followed by addition DI water with the mass ratio (DI water/PEG) of 0.5, then stirred for a further 20 min to obtain a homogeneous solution and transferred into a 100 mL Teflon-lined stainless steel autoclave. The autoclave was sealed and maintained at 200 ^{o}C for 6 h in a blast oven, then cooled to ambient temperature. The precipitate was collected and washed with absolute ethanol for several times by vacuum filtration, and finally dried at 60 ^{o}C. In order to study CoMn$_2$O$_4$ spinel with different degree of crystallinity, the dried precipitate was further calcined in air for 6 h at various temperatures, including 250 ^{o}C, 300 ^{o}C, 400 ^{o}C, 500 ^{o}C, and 600 ^{o}C.

Characterizations

The crystalline structures are characterized by XRD (Rigaku D/max 2500PC system) with Cu-Ka radiation (λ = 0.15418 nm) in the 2 Theta range between 10º and 90º with scan rate of 8º min$^-$^{1}. Field emission scanning electron microscopy (FE-SEM, Hitachi S4700, 15 kV) and Transmission electron microscope (TEM, JEOL JEM-2100F) are employed for surface morphology assessment. Thermo gravimetric analysis (TGA) and Differential Scanning Calorimetry (DSC) (TA instruments, Q500) was carried out using a temperature ramp of 10 ^{o}C min^{-1} under an open air atmosphere.

Electrochemical measurements

The working electrodes were prepared by mixing the spinel CoMn$_2$O$_4$ material with acetylene black and polite trafluorene-ethylene binder (diluted from 60 wt.% to 5 wt.%) at a mass ratio of 80: 15: 5. A small amount of absolute ethanol was added to the mixture to produce a homogeneous paste. The mixture paste was dried at 60 ^{o}C for 2 h before coated on a nickel foam current collectors as working electrode. The electrochemical performance of the as-prepared electrode are measured with a conventional three-electrode cell with 1 M Na$_2$SO$_4$ as the electrolyte, platinum foil and saturated calomel electrode (SCE) as the counter and reference electrodes, respectively. All electrochemical measurements were conducted on a electrochemical workstation (CHI 760D, CH Instrument, China).

Results and discussion

Characterizations of CoMn$_2$O$_4$ flower-like microspheres

The SEM and TEM morphologies of CoMn$_2$O$_4$ powders are displayed in Fig. 1. The powders were calcined at 300 ^{o}C. From the SEM pictures (Fig. 1a and Fig. 1b), we can see that the final product is composed of uniform and discrete microspheres with size of ~3 μm. Each microsphere is constructed from numerous cross-linked nanosheets (Fig. 1c), intersected in a flower like morphology, as shown in Fig. 1c. More importantly, no agglomeration is observed. Further TEM characterization (Fig. 1d

and Fig. 1e) indicates that the pores are interlinked and exist in the whole microspheres, from the outer surface to the inner center, implying a large internal surface area of the microsphere structure. The thickness of these nanosheets is between 25 nm to 50 nm. The selected area electron diffraction (SAED) pattern exhibits the polycrystalline nature of MnCo$_2$O$_4$. However, the ring is not well-defined, indicating the microspheres are not well crystallizated at 300 ^{o}C clacination. Through a N$_2$ absorption measurement at 77 K, the flower-like microspheres structure contributed to a BET surface area of 16 m^2 g^{-1} (Fig. S1), and the mean diameter of the pore size is ~5nm according to BJH method.
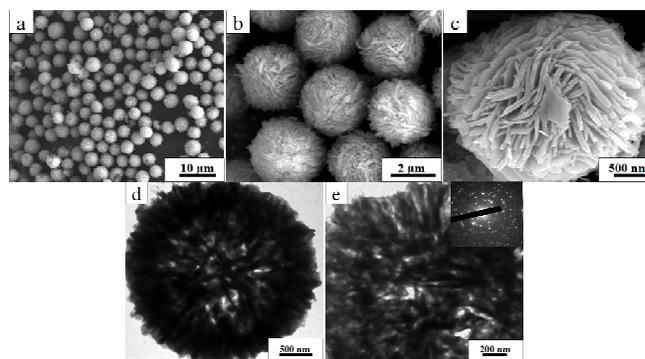
Fig. 1 SEM surface morphologies (a, b and c) and TEM images of the CoMn$_2$O$_4$ microsphere (d and e).
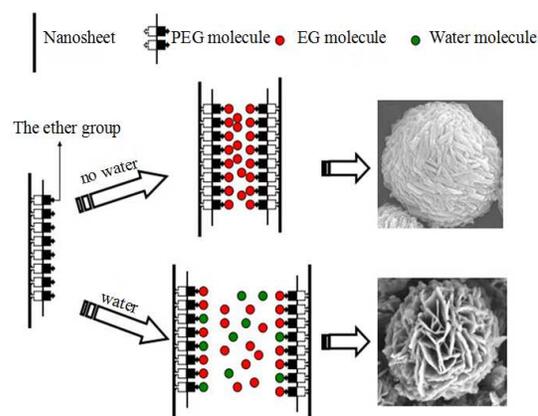
Fig.2 The schematic show of flower-like microspheres formation mechanism

In a typical solvothermal reaction of EG with metal salts, the products can be ascribed to the formation of metal glycolates or alkoxide derivatives by alcoholysis and coordination of with the cations [27-29]. Here we used Co/Mn-EG for simplication. The effect of small amount of DI water additive was also studied. In the solvothermal reaction of Co/Mn-EG precursor, the reaction process is shown in Fig. 2. When nanosheets are formed, PEG molecules will stick on the surfaces as the interaction of Van der Waals forces, electrostatic force and hydrogen bonds. The outer layer mainly constructed with the polar ends (the ether group) of PEG molecules, which have strong affinity with polar molecules. When no DI water is involved, the outer layer is completely covered by EG molecules; the electrostatic repulsion between nanosheets is very small in such uniform environment, leading to

a negligible gap between the two nanosheets. Moreover, the uniform outer layer will make nanosheets easily grown in the transverse direction, finally form a thick nanosheet.

In addition, as the polar ends of PEG molecules have both affinities for water and EG molecules, once DI water was involved into the reaction, the outer layer will be partially covered by water molecule. By increasing the DI water content, the mixed environment will increase the electrostatic repulsion and the steric effect of PEG molecules between nanosheets. Moreover, when heated to 200 ^{o}C, the small amount of DI water should be presented as gas phase, the active water vapor will hinder the compact packing of the nanosheets, which leads to the flower-like microspheres instead of compact ones [30].
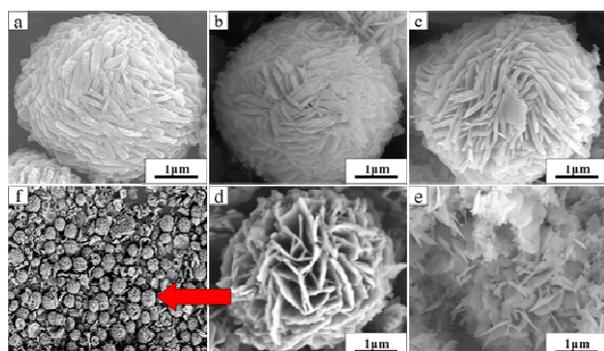
Fig. 3 SEM images of the final CoMn$_2$O$_4$ spinel materials in solvothermal process with different DI water content: (a) 0 ml, (b) 0.25 ml, (c) 0.5 ml, (d) 1 ml and (e) 1.5 ml; (f) lower magnification of image (d).

In order to confirm the effects of DI water on the microsphere morphology, SEM morphologies are studied for the samples with different amount of DI water addition. Fig. 3 is the SEM image of the corresponding samples, which showed the morphology evaluation when the DI water mass ratio with PEG varied from 0, 0.2, 0.5, 1 to 1.5, respectively. When no water is involved (mass ratio is 0), the morphology of microspheres is solid balls composed by closely packed nanosheets, with nearly no internal holes (Fig. 3a). As the amount of DI water increasing, the internal gaps between nanosheets start to show up to form the blooming like flower shape. The more DI is introduced, the larger gaps between nanosheets will be (from Fig. 3b to Fig. 3d). With further increasing the mass ratio reach to 1.5, the microsphere collapses as Fig. 3(e). To double check the morphologies of Fig. 3d at lower magnification, the microspheres are distributed with collapsed nanosheets, as Fig. 3f, so the microspheres are not uniform. Overall, with DI water mass ratio was below 0.5, microspheres with uniform distribution could be obtained. In the aspect of surface area and uniform microsphere structure, we choose the recipe with mass ratio 0.5 (Fig. 3c) as the optimized result for further material and electrochemical characterization.

Moreover, it is noted that the nanosheet thickness becomes thinner with the DI content increasing, illustrating that the dispersion effect represented well in all aspects of the mechanism (Fig. 2).
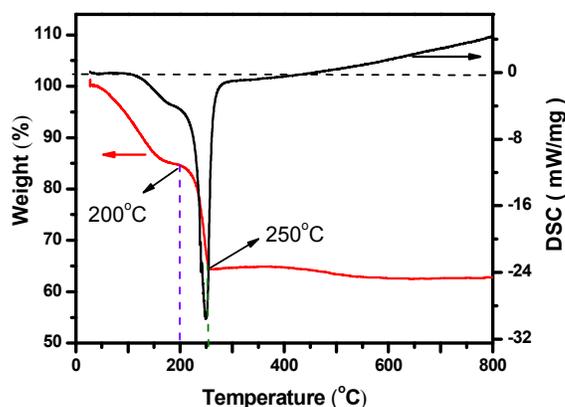
Fig. 4 TGA/DSC curves for the precursor Co/Mn-EG in air
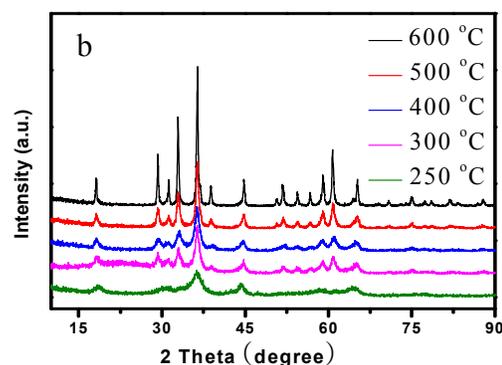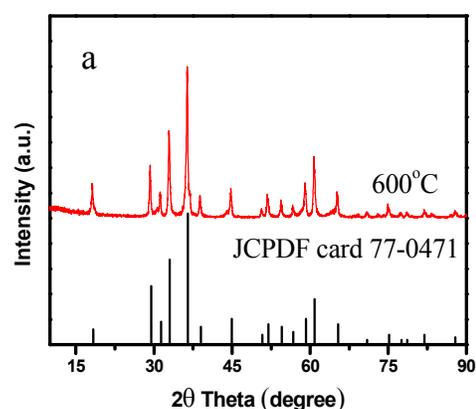
Fig. 5 (a) XRD patterns of CoMn$_2$O$_4$ microspheres after calcination at 600 ^{o}C for 6 h; (b) XRD patterns of CoMn$_2$O$_4$ microspheres after calcination at different temperatures.

The pyrolysis behavior of the precursor (Co/Mn-EG) was investigated by TGA/DSC, as demonstrated in Fig. 4. The whole process can be categorized into three major weight loss steps. The first step under 200 ^{o}C was the loss of the physically and chemically adsorbed water. In the second step, the sharp weight loss occurs in the temperature range of 200 ^{o}C ~250 ^{o}C, which is attributed to the combustion of ethylene glycol, convinced by the DSC curve since much more heat was absorbed in this range.

Finally, when the temperature further rises from 250 °C to 600 °C, only slight weight loss occurs and the DSC data showed an exothermic process, which is attributed to the process of further crystallization, and calcination process may lead to a porous
5 structure [31, 32]. In order to study temperature effect on $CoMn_2O_4$ spinel, the dried precipitate was calcined at various temperatures, including 250 °C, 300 °C, 400 °C, 500 °C, and 600 °C.

XRD was conducted to study the effect of calcination temperatures on the $CoMn_2O_4$ structure, as shown in Fig. 5. Fig.
10 5a compared $CoMn_2O_4$ sample (calcined at 600 °C) with the PDF card (JCPDF card 77-0471), from which all the diffraction peaks can be indexed and assigned to $CoMn_2O_4$ phase without any impurities.

Fig. 5b shows the XRD patterns of the samples after
15 calcination at temperature of 250 °C, 300 °C, 400 °C, 500 °C and 600 °C. It reveals that the spinel structure can be completely achieved at 300 °C. With the increase of temperature, the sharp and well-defined peaks on the diffractogram implying higher crystallinity. However, only several wide and weak peaks
20 displayed at 250 °C, suggesting the powder is not fully crystallized.

Electrochemical properties of $CoMn_2O_4$ microspheres electrode

Fig. 6 presents the CV curves of the $CoMn_2O_4$ microspheres
25 after calcinations at various temperatures, measured in three-electrode system at the scan rate of 20 mV s^{-1}. All the CV curves exhibit nearly rectangular shape, indicating the ideal capacitive behavior and fast charging/discharging process characteristic for the obtained samples. For oxides materials in pseudocapacitor,
30 the crystallinity is an important factor mainly reflected in the balance between electrical conductivity and ionic transportation.
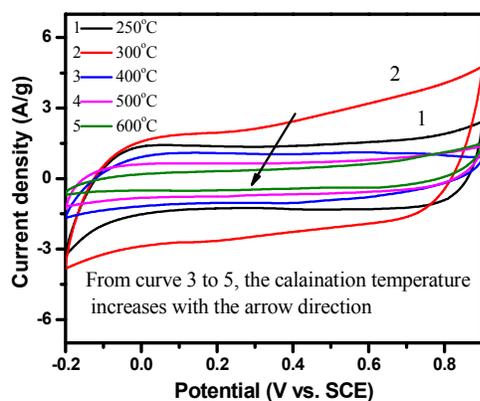
Fig. 6 CV curves of the $CoMn_2O_4$ microspheres after calcinations at different temperatures at the scan rate of 20 mV s^{-1}.

35 Typically, well crystallized structure limits the ions diffusion because lattice expansion or contraction is restricted strictly, accordingly the charge transfer resistance increases. As a result, for the materials calcined at higher temperatures, the active sites numbers decreases with the crystallization degree, so the specific
40 capacitance of electrode materials will be affected negatively. On the other hand, too low crystallinity leads to a low conductivity

[33-35]. The principle can be applied for $CoMn_2O_4$ spinel material, as shown in Fig. 6. The current density increases with increasing calcinations temperature from 250 °C to 300 °C, then decreases
45 with the further increasing the calcinations temperature to 600 °C, indicating that the 300 °C sample gives the relatively highest specific capacitance. Therefore, 300 °C was used as the optimized calcination temperature for further study.

Based on the literatures of Mn-Co oxides in aqueous
50 electrolyte [13, 36], the redox reaction mechanism for the pseudocap-acitance of the $CoMn_2O_4$ composite oxide is described by Eq. 1 and 2 as follows.

$$CoMn_2O_4 + H_2O + OH^- \rightarrow CoOOH + 2MnOOH + e \quad (1)$$

$$MnOOH + CoOOH + OH^- \rightarrow MnO_2 + CoO_2 + H_2O + 2e \quad (2)$$
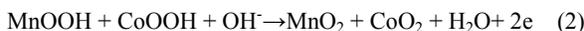
55 The reactions are highly reversible. Fig. 7a presents the CV curves of the sample that calcined at 300 °C at different scan rates (from 5 mV s^{-1} to 50 mV s^{-1}) in a potential window of -0.2 ~ 0.9 V (vs. SCE). It is worth noting that all the CV curves of the spinel $CoMn_2O_4$ material exhibited close to a rectangular shape, which
60 is typical shape for supercapacitor in neutral electrolyte [37], and desirable for an ideal supercapacitor. The rectangular area increased with increasing the scan rate. In addition, the electrode can remain stable at much larger potential window than that in alkaline electrolyte, which is typical less than 0.6 V [38-40].

65
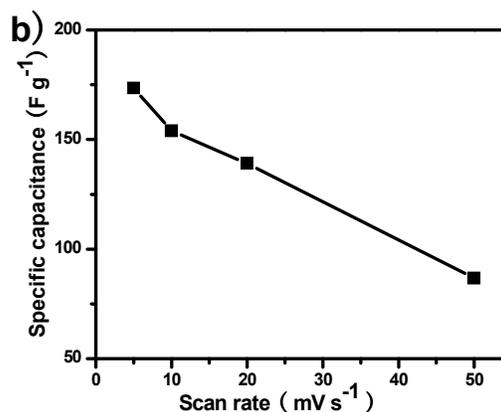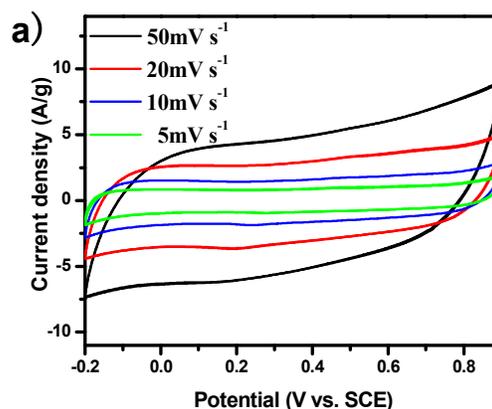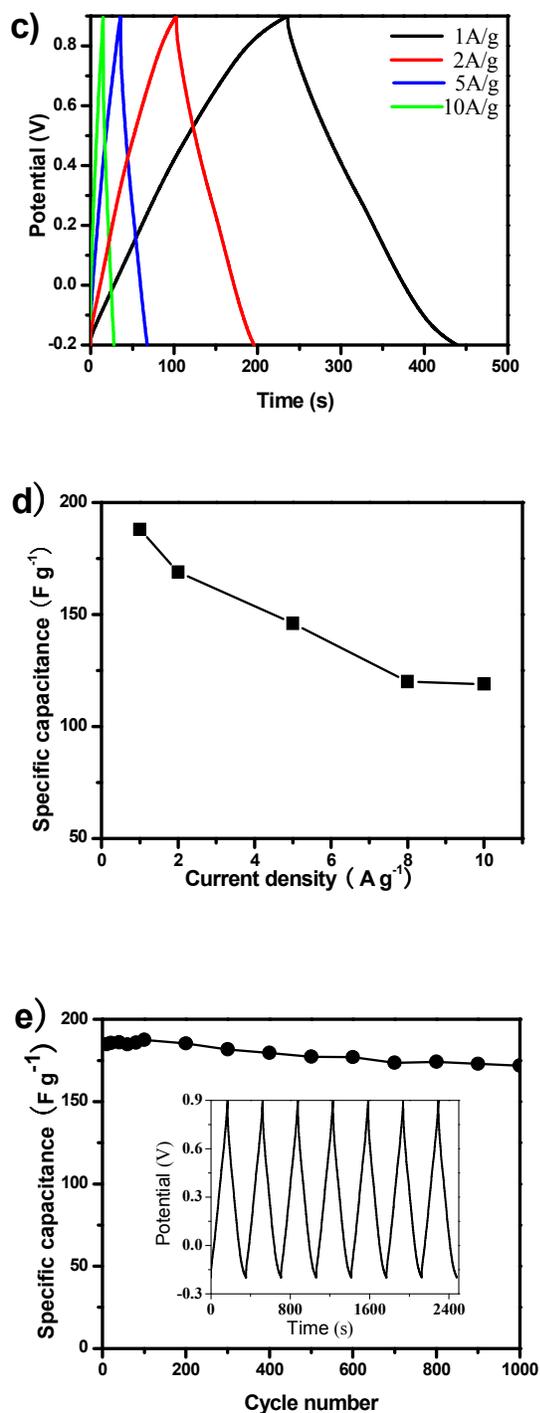
Fig. 7 Electrochemical characterizations of the CoMn$_2$O$_4$ flower-like microspheres as electrodes for supercapacitors. The materials were calcined at 300 ^{o}C：a) CV curves at various scan rates ranging from 5 to 50 mV s^{-1}; b)The calculated capacitance as a function of scan rate; c) charge/discharge voltage profiles at various current densities ranging from 1 to 10 A g^{-1}; d) the calculated capacitance as a function of current density; e) the capacitance as a function of cycle number at constant current densities of 1 A g^{-1} for 1000 cycles.

Fig. 7c depicts the galvanostatic charge/discharge behaviors of the electrodes between -0.2 V and 0.9 V at different current densities, which presents ideal linear behavior with good symmetry. For most materials, the specific capacitance decreases with the increasing of discharge current density, which comes from two reasons. Firstly, assuming the resistance is constant, high current density suggests high potential drop, so low capacitance is inevitable, as proved in the CVs when scan rate increased (Fig. 7b). Secondly, when the current density is low, ions have sufficient time to penetrate into the inner-structure of electrode material, being able to access to more internal pores of the electrode. While at higher current densities, the charging/discharging time is short, so that part of the internal surfaces of electrode materials cannot be effectively utilized; the retained capacitance only come from the electrochemical process on the outer surface, the capacitances are decreased accordingly. The effect is more obvious for porous materials.

The specific capacitance can be calculated according to the following Eq. 3:

$$C = \frac{I}{m} \bullet \frac{\Delta t}{\Delta V} \qquad (3)$$

Where I is the discharge current density, m is the mass of the applied active materials of the working electrode, ΔV is the working potential range, and Δt represents the discharging time. The calculated specific capacitances as a function of the discharge current densities are plotted in Fig. 7d, the specific capacitances are 188 F g^{-1}, 169 F g^{-1}, 146 F g^{-1}, 120 F g^{-1} and 119 F g^{-1} at the current densities of 1 A g^{-1}, 2 A g^{-1}, 5 A g^{-1}, 8 A g^{-1} and 10 A g^{-1}, respectively. The specific capacitance can retain about 63.3% with the increased current density from 1 A g^{-1} to 10 A g^{-1}, which is much higher than the recent similar reports measured in neutral electrolyte for CoMn$_2$O$_4$[41]. In addition, the cycling stability is also evaluated by the consequent charging-discharging measurement at a constant current density of 1 A g^{-1}, as shown in Fig. 7e. After 1000 cycles, the electrode retained 93% of the original capacitances.

At low scan rate like 5mV s^{-1} the specific capacitance is 174 F g^{-1} (Fig. 7b). The specific capacitance will decreases as the scan rate increases just like most any other materials. However, even at the scan rate reach to 50 mV s^{-1}, the specific capacitance can remain 87 F g^{-1} as show in Fig 7b. The results demonstrate that the polyporous active material performs a high rate capability in 1M Na$_2$SO$_4$.

Furthermore, the reaction kinetics can be evaluated by EIS test. The Nyquist plots of the electrode had been compared for the fresh one, after 500, and 1000 cycles, as shown in Figure 8. Each plot consists of a semicircle at high frequency region and an inclined line in the low-frequency region.

The intercept on the Z real axis in the high-frequency region corresponds to equivalent series resistance (ESR, R$_s$), including the inherent resistances of the electrode, bulk resistance of electrolyte, and contact resistance at the interface between electrolyte and electrode. The semicircle in the middle frequency range indicates the charge-transfer resistance (R$_{ct}$) through the interface [42]. The inclined straight line in the low frequency corresponds to Warburg impedance related to the diffusion of electrolyte within the electro active materials. Here the R$_s$ are 5.8, 6.1 and 6.3 Ω for the fresh electrode, after 500 cycles and 1000

cycles, respectively. The semicircle diameter reflecting R_{ct} was calculated to be 20.2, 26.4 and 25.5 Ω for the fresh electrode, after 500 cycles and 1000 cycles, respectively. This indicates there is only a small change of the R_s and R_{ct} between 500cycles and 1000 cycles. The ion diffusion resistances indicated by the inclined line of Nyquist plots also presented the nearly overlapping line. This proves the stable cycling performance of electrode. In addition, the diffusive resistance (Warburg impedance) was a little higher after 500 and 1000 cycles in lower frequencies. These results may be because the surface and microstructure changes of the $CoMn_2O_4$ electrodes after 1000 successive cycles.
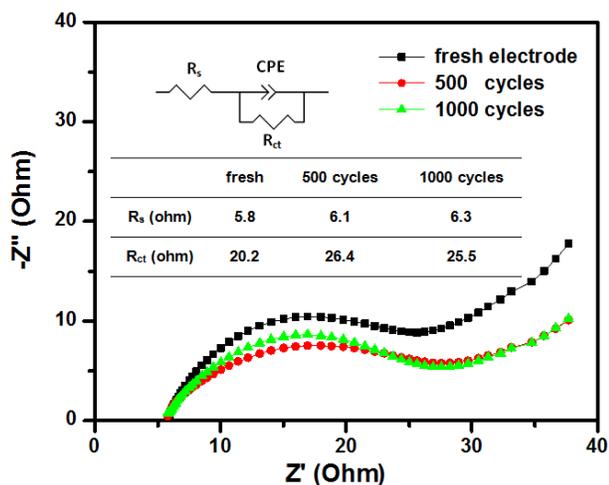
Fig.8 Nyquist plots of the fresh electrode and the ones after 500, 1000 cycles.

Meanwhile, the straight line showed less vertical shape comparing with $(Mn,Co)_3O_4$ spinels in KOH electrolyte [22, 23], because Na_2SO_4 electrolyte displayed lower molar conductivity, with larger hydration spheres of Na^+ and less molar conductivity of SO_4^{2-}. However, the high overpotential for dihydrogen evolution results in higher potential window. Therefore, electrolyte of Na_2SO_4 displayed lower specific capacitance with larger potential window.

Conclusions

This work demonstrated a facile method for the synthesis of the flower-like $CoMn_2O_4$ microspheres for supercapacitor electrode applications，including a low temperature solvent thermal and following calcinations processes. In the solvothermal process, DI water content plays a key role in controlling the nanosheet gaps of flower-like microspheres structure. The following calcination temperature was optimized to obtain the highest specific capacitances.

In 1 M Na_2SO_4 neutral solution, the spinel electrode material exhibited a working voltage as high as 1.1 V and a specific capacitance of 188F g^{-1} was obtained at the current density of 1 A g^{-1}. The electrode material showed excellent cycling stability by retaining 93% of their maximum capacitance after 1000 cycles. EIS further proved the good cycle performance by presenting little charge transfer resistance change from 500 to 1000 cycles. These achievements enriched the research direction and application potential for spinel materials in supercapacitor electrodes.

Notes and references

1. *Department of Materials Science and Engineering, Harbin Institute of Technology Shenzhen Graduate School, Shenzhen Key Laboratory of Advanced Materials, Shenzhen 518055, China. Fax: 86-755-2603 3504; Phone: 86-755-2603 3290; junwei.wu@hitsz.edu.cn*
2. Department of Applied Chemistry, Tianjin Polytechnic University, Tianjin 300387, China
3. Department of Materials Science and Engineering, Zhejiang University, Hangzhou 310027, China
4. Dongguan McNair Technology Co., Ltd, Dongguan City, Guangdong 523700, China

1   M. Zhi, C. Xiang, J. Li, M. Li and N. Wu, *Nanoscale*, 2013, **5**, 72-88.
2   R. Kötz and M. Carlen, *Electrochim. Acta*, 2000, **45**, 2483-2498.
3   F. Béguin, V. Presser, A. Balducci and E. Frackowiak, *Adv. Mater.*, 2014, **26**, 2219-2251.
4   Y. Zhang, H. Feng, X. Wu, L. Wang, A. Zhang, T. Xia, H. Dong, X. Li and L. Zhang, *Int. J. Hydrogen Energy*, 2009, **34**, 4889-4899.
5   L. L. Zhang and X. S. Zhao, *Chem. Soc. Rev.*, 2009, **38**, 2520-2531.
6   E. Frackowiak and F. Beguin, *Carbon*, 2001, **39**, 937-950.
7   J. R. Miller and P. Simon, *Science*, 2008, **321**, 651-652.
8   J. Zhao, C. Lai, Y. Dai and J. Xie, *Mater. Lett.*, 2007, **61**, 4639-4642.
9   A. Jänes, H. Kurig and E. Lust, *Carbon*, 2007, **45**, 1226-1233.
10   M. Liu, J. Chang, J. Sun and L. Gao, *RSC Adv.*, 2013, **3**, 8003-8008.
11   H. Xia, Y. S. Meng, G. Yuan, C. Cui and L. Lu, *Electrochem. Solid-State Lett.*, 2012, **15**, A60-A63.
12   D. Yan, Z. Guo, G. Zhu, Z. Yu, H. Xu and A. Yu, *J. Power Sources*, 2012, **199**, 409-412.
13   C. Xiang, M. Li, M. Zhi, A. Manivannan and N. Wu, *J. Power Sources*, 2013, **226**, 65-70.
14   X. Du, C. Wang, M. Chen, Y. Jiao and J. Wang, *J. Phys. Chem. C*, 2009, **113**, 2643-2646.
15   Y. Chen, C. Liu, F. Li and H. Cheng, *J. Alloy Compd.*, 2005, **397**, 282-285.
16   Q. Wang, J. Xu, X. Wang, B. Liu, X. Hou, G. Yu, P. Wang, D. Chen and G. Shen, *ChemElectroChem*, 2014, **1**, 559-564.
17   B. Liu, J. Zhang, X. Wang, G. Chen, D. Chen, C. Zhou and G. Shen, *Nano Lett.*, 2012, **12**, 3005-3011.
18   H. Jiang, J. Ma and C. Li, *Chem. Commun.*, 2012, **48**, 4465-4467.
19   S. Kim, H. Lee, P. Muralidharan, D. Seo, W. Yoon, D. K. Kim and K. Kang, *Nano Res.*, 2011, **4**, 505-510.
20   L. Zhou, D. Zhao and X. W. Lou, *Adv. Mater.*, 2012, **24**, 745-748.
21   H. B. Wu, H. Pang and X. W. D. Lou, *Energy Environ. Sci.*, 2013, **6**, 3619-3626.
22   Y. Xu, X. Wang, C. An, Y. Wang, L. Jiao and H. Yuan, *J. Mater. Chem. A*, 2014, **2**, 16480-16488.
23   W. Li, K. Xu, G. Song, X. Zhou, R. Zou, J. Yang, Z. Chen and J. Hu, *CrystEngComm*, 2014, **16**, 2335-2339.
24   K. Fic, G. Lota, M. Meller and E. Frackowiak, *Energy Environ. Sci.*, 2012, **5**, 5842-5850.
25   Q. Qu, P. Zhang, B. Wang, Y. Chen, S. Tian, Y. Wu and R. Holze, *J. Phys. Chem. C*, 2009, **113**, 14020-14027.

26 L. Hu, H. Zhong, X. Zheng, Y. Huang, P. Zhang and Q. Chen, *Sci. Rep.*, 2012, **2**, 1-8

27 A. Cao, J. D. Monnell, C. Matranga, J. Wu, L. Cao and D. Gao, *J. Phys. Chem. C*, 2007, **111**, 18624-18628.

5 28 X. Jiang, Y. Wang, T. Herricks and Y. Xia, *J. Mater. Chem.*, 2004, **14**, 695-703.

29 D. Larcher, G. Sudant, R. Patrice and J. Tarascon, *Chem. Mater.*, 2003, **15**, 3543-3551.

30 L. Li, Y. Cheah, Y. Ko, P. Teh, G. Wee, C. Wong, S. Peng and M. Srinivasan, *J. Mater. Chem. A*, 2013, **1**, 10935-10941.

31 Y. Zhang, Y. Wang, Y. Xie, T. Cheng, W. Lai, H. Pang and W. Huang, *Nanoscale*, 2014, **6**, 14354-14359.

32 H. Pang, J. Deng, J. Du, S. Li, J. Li, Y. Ma, J. Zhang and J. Chen, *Dalton Trans.*, 2012, **41**, 10175-10181.

15 33 G. Wang, L. Zhang and J. Zhang, *Chem. Soc. Rev.*, 2012, **41**, 797-828.

34 L. Mao, K. Zhang, H. S. O. Chan and J. Wu, *J. Mater. Chem.*, 2012, **22**, 1845-1851.

35 M. Ramani, B. S. Haran, R. E. White and B. N. Popov, *J. Electrochem. Soc.*, 2001, **148**, A374-A380.

36 L. Zhao, J. Yu, W. Li, S. Wang, C. Dai, J. Wu, X. Bai and C. Zhi, *Nano Energy*, 2014, **4**, 39-48.

37 J. Chang, W. Hsieh and W. Tsai, *J. Alloy. Compd.*, 2008, **461**, 667-674.

25 38 L. Li, Y. Q. Zhang, X. Y. Liu, S. J. Shi, X. Y. Zhao, H. Zhang, X. Ge, G. F. Cai, C. D. Gu and X. L. Wang, *Electrochim. Acta*, 2014, **116**, 467-474.

39 S. Jiang, T. Shi, H. Long, Y. Sun, W. Zhou and Z. Tang, *Nanoscale Res. Lett.*, 2014, **9**, 1-8.

30 40 L. Kong, C. Lu, M. Liu, Y. Luo, L. Kang, X. Li and F. C. Walsh, *Electrochim. Acta*, 2014, **115**, 22-27.

41 P. Ahuja, V. Sahu, S. K. Ujjain, R. K. Sharma and G. Singh, *Electrochim. Acta*, 2014, **146**, 429-436.

42 R. B. Rakhi, W. Chen, D. Cha and H. N. Alshareef, *Nano Lett.*, 2012, **12**, 2559-2567.